THE JOURNAL OF PHYSICAL CHEMISTRY C

pubs.acs.org/JPCC Article

Extraordinary Electromechanical Actuation of Ti_2C MXene

Bozhao Wu, Xiaoxi Cai, Langquan Shui, Enlai Gao,* and Ze Liu

Cite This: J. Phys. Chem. C 2021, 125, 1060−1068 Read Online

ACCESS | Metrics & More | Article Recommendations | Supporting Information

ABSTRACT: Two-dimensional transition-metal carbides and nitrides, often known as MXenes, have fantastic properties benefiting from their unique structures, enabling them to be used in many applications. In this work, we show that Ti_2C MXene possesses extraordinary electromechanical actuation performance using first-principles calculations. Upon charge injection, the maximum uniaxial and biaxial isometric actuation stresses are 31.1 (along the armchair direction) and 75.6 GPa, respectively, and the maximum isobaric actuation strain is 27.4%. More importantly, the electromechanical actuation of Ti_2C MXene is in-plane isotropic because of the 3-fold rotational symmetry, and the in-plane area can be stimulated to increase by 62.2%, which is greater than other well-known two-dimensional materials. The maximum realistic gravimetric work density of Ti_2C MXene is also extraordinary (1271.6 J/g). Finally, the mechanism for the extraordinary electromechanical actuation performance of Ti_2C MXene was elucidated by the analyses at atomic and electronic scales. Additionally, mechanical tests show that the structural integrity of Ti_2C MXene can be well maintained under a certain amount of electromechanical loads. Our findings indicate that Ti_2C MXene can be used for high-performance nanoelectromechanical actuators.

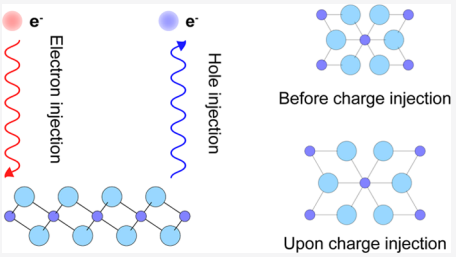

INTRODUCTION

Stimuli-responsive materials (SRMs) can change one or more of their properties under a defined stimulus. The external stimuli for material responses include heat,[1,2] electric field,[3] magnetic field,[4,5] and electrostatic force.[6,7] Electromechanical actuation materials, as one of the most important members of SRMs, have been studied as actuators that can convert electrical energy into mechanical energy.[8−14] Since carbon nanotube (CNT) sheets were found to exhibit a remarkable actuation upon immersion in an aqueous electrolyte by Baughman et al.,[15] developing artificial muscles to mimic the behaviors of mammalian skeletal muscle has attracted considerable attention.[2,16−19] However, it is a long-term challenge to develop such actuators that can perform reversible large strokes, significant actuation stress, and high work densities,[1−3,16,20] like natural muscles under complex loads.[21,22] These issues limit many exciting applications of material-based actuators, such as micro/nanoelectromechanical systems, flexible robotics, and artificial joints and organs.[16,23−26]

Actuators based on a host of materials have been previously studied.[15,19,27−31] With the discovery of two-dimensional materials (2DMs) and the increasing demand for nanoactuators,[32] a few 2DM-based actuators have arisen, such as transition-metal dichalcogenides (TMDs),[33−35] graphene-based materials,[36−47] and black phosphorene (BP).[48] Liu et al.[42,45,47] first studied the electromechanical actuation performance of graphene and its derivatives (graphene oxide) as 2DM-based actuators in theory and found that graphene oxide with ordered epoxy groups possesses a maximum recoverable strain of 14.5%, resulting from a reversible phase transition.[46] Wu et al.[48] revealed that black phosphorene (BP) can exhibit a stroke as high as 36.6% upon charge injection and a high volumetric work density (207.7 J/cm^3).

Discovered at Drexel University,[49,50] 2D transition-metal carbides and nitrides, often known as MXenes, have emerged for use in many applications, such as energy storage and conversion,[51−53] reinforced composites,[54−56] water purification,[57] catalysis,[58] and photothermal conversion.[59,60] The variety of compositions and structures of MXenes has led to a rapidly expanding family of 2D materials.[60] Ti_2C MXene, as one of the most important members of MXene family, has an in-plane isotropic stiffness of approximately 130 N/m[61,62] and a strain to failure of about 13%.[63] In addition, Ti_2C MXene shows a durable performance during the charge/discharge procedure for the application of lithium-ion battery.[64] The unique structure suggests the possibility of MXenes for use in high-performance nanoelectromechanical actuators. Additionally, hole doping (positive charging) of MXenes has been explored in experiments as demonstrated in some works on MXene-based electroactive ionic actuators,[65−68] which further suggests the possibility of high actuation performance of MXene. However, the electromechanical actuation performance of MXenes has not been examined.

Received: October 20, 2020
Revised: December 7, 2020
Published: December 23, 2020

https://dx.doi.org/10.1021/acs.jpcc.0c09482
J. Phys. Chem. C 2021, 125, 1060−1068

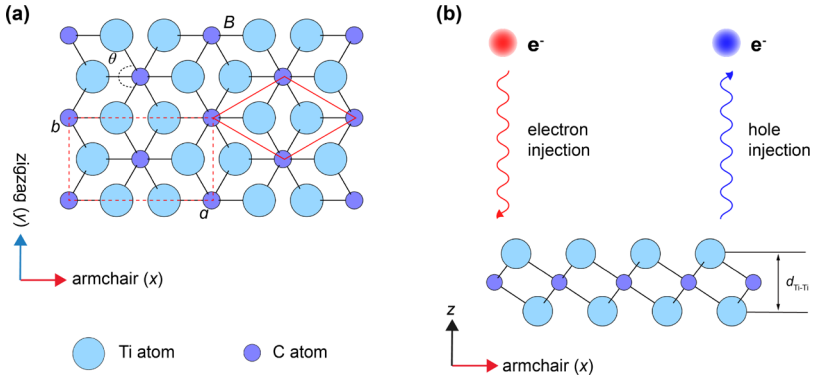

Figure 1. Computational models for Ti_2C MXene. (a) Atomistic structure of Ti_2C MXene (top view). The red solid and dashed boxes are the primitive and rectangular cells of Ti_2C MXene, respectively. (b) Illustration of Ti_2C MXene upon charge injection (side view). B, θ, and d_{Ti-Ti} are the bond length of Ti−C, bond angle of Ti−C−Ti, and atomic distance of Ti_2C MXene, respectively.

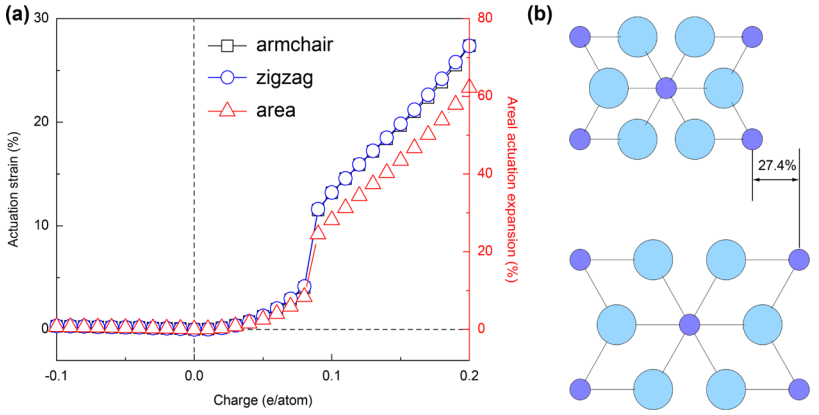

Figure 2. Electromechanical actuation strain of Ti_2C MXene upon charge injection. (a) Actuation strain and areal actuation expansion as a function of charge injection. (b) Atomistic structures of Ti_2C MXene before and after hole injection of 0.20 e/atom.

Herein, we explored the electromechanical actuation performance of Ti_2C MXene using first-principles calculations. Upon charge injection, it shows extraordinary mechanical responses including the maximum isobaric actuation strain of 27.4%, the maximum uniaxial (biaxial) isometric actuation stress of 31.1 (75.6) GPa, and the maximum realistic gravimetric work density of 1271.6 J/g. More importantly, the large in-plane isotropic actuation strain results in an increase of area by 62.2%, which is much greater than already-known 2D materials. The mechanism for the extraordinary electromechanical actuation of Ti_2C MXene was uncovered by analyses at atomic and electronic scales. Additional calculations confirm that Ti_2C MXene can well maintain the structural integrity upon a certain amount of electromechanical loads.

METHODS

To investigate the electromechanical actuation of Ti_2C MXene, first-principles calculations were performed using the Vienna Ab initio Simulation Package (VASP).[69,70] Perdew−Burke−Ernzerhof[71] of the generalized gradient approximation[72] was used for the exchange-correlation functional. DFT-D3 method of Grimme[73] was used to treat the van der Waals (vdW) correction. To ensure accuracy, an energy cutoff of 520 eV was adopted in all calculations. The k-point sampling with the density >40 Å (the product of each lattice constant and the corresponding number of k-points) adopted the Monkhorst−Pack scheme.[74] To eliminate electrostatic interactions, a thick interlayer spacing of 70 Å was used. All structures were relaxed to their ground state before and after charge injection using the quasi-Newton algorithm. For geometry relaxation, the force on each atom was converged below 0.001 eV/Å. To achieve a constant vacuum spacing while the cell can be optimized in the basal plane, the VASP code was modified. Considering the 2D character of the simulated 2D materials, the value of the actuation stress should be rescaled by z/d (z is the cell length along the vacuum direction, and d is the effective thickness of the Ti_2C MXene). The effective thickness (d) of Ti_2C MXene can be obtained as the interlayer distance between optimized bilayer Ti_2C MXene, and herein d of 4.828 Å[64] was used for calculating the actuation stress.

RESULTS AND DISCUSSION

The primitive (red solid box) and rectangular cells (red dashed box) of Ti_2C MXene are shown in Figure 1a. Before charge injection, the optimized lattice parameters are a = 5.22 Å and b = 3.01 Å. The bond length of Ti−C (B), bond angle of Ti−C−Ti (θ), and atomic distance (d_{Ti-Ti}, the distance between top and bottom layers of Ti atoms) are 2.09 Å, 92.18°, and 2.32 Å, respectively. The electromechanical responses of Ti_2C MXene were investigated using the computational setup as illustrated in Figure 1b, in which the rectangular cell was used in first-principles calculations.

Actuation Strain. Actuation strain was measured as the change of in-plane lattice constants after charge injection divided by their original values before charge injection. Upon electron injection, Ti_2C MXene shows a slight actuation strain

https://dx.doi.org/10.1021/acs.jpcc.0c09482
J. Phys. Chem. C 2021, 125, 1060−1068

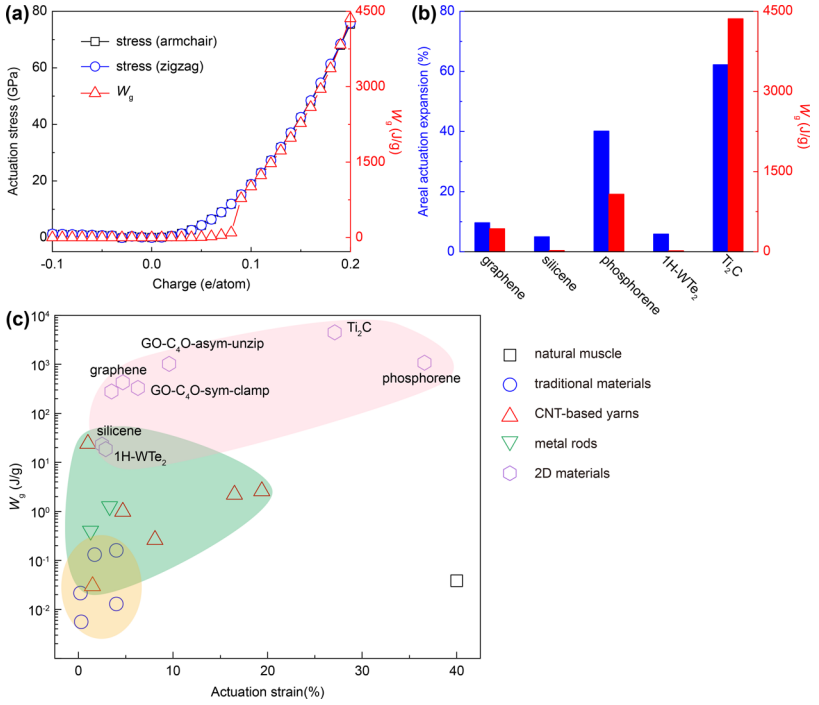

Figure 3. Electromechanical actuation stress and work density of Ti_2C MXene. (a) Actuation stress and gravimetric work density (W_g) as a function of injected charge. (b) Comparison of the maximum areal actuation expansion and gravimetric work density (W_g) of Ti_2C MXene with other 2D materials. (c) Actuation strain and W_g of Ti_2C MXene as compared with typical actuation materials. The original data can be found in Table S1. For a fair comparison, we used the nominal work density to compare with the ones reported in the literature.

of 0.3% (0.4%) in the armchair (zigzag) direction, similar to those of graphene and BP.[42,48] However, upon hole injection, the maximum actuation strain of Ti_2C MXene can be as high as 27.4% (Figure 2a and Movie S1). The in-plane actuation strain of Ti_2C MXene is isotropic, resulting from the 3-fold rotational symmetry of Ti_2C MXene. Figure 2b shows the atomistic structures of Ti_2C MXene before and after hole injection of 0.20 e/atom. Compared with other 2D materials (Figure S1a), the maximum actuation strain of Ti_2C MXene is 4.3 times larger than that of some graphene oxide compounds (6.3%)[42] but smaller than that of BP (36.6%).[48] Meanwhile, the areal actuation expansion (the change of in-plane area after charge injection divided by the original value before charge injection) as a function of injected charge was calculated and compared with other 2D materials (Figures 2a and S1b; see Section 1 of the Supporting Information for details). The calculated maximum areal actuation expansion of Ti_2C MXene is 62.2%, which is much larger than other 2D materials. Notably, although BP shows a high actuation strain along the armchair direction (36.6%),[48] the actuation strain along the zigzag direction is quite small (2.6%) due to its extremely large mechanical anisotropy, which results in a smaller areal actuation expansion of BP (40.1%) than Ti_2C MXene (62.2%). The areal actuation expansion of 2D materials plays an important role in applications of microelectromechanical systems (MEMS) actuators or switches,[75−77] such as a membrane valve actuator that can control the flow of fluids in microfluidic channels and a mechanical switch that can control the light into a device.[78]

Actuation Stress and Work Density. Furthermore, actuation stress and work density as a function of charge injection were investigated. Upon charge injection, the isometric actuation stress of Ti_2C MXene was measured by fixing the in-plane lattice constants of Ti_2C MXene at their original values before charge injection. As shown in Figure 3a, the actuation stress as a function of injected charge along the armchair and zigzag directions is almost isotropic. Upon hole injection of 0.20 e/atom, the actuation stress in the armchair and zigzag directions is as high as 75.4 and 75.8 GPa (75.6 GPa on average). While injecting electrons, a low isometric actuation stress below 1.3 GPa is observed. In addition, we also measured the uniaxial actuation stress upon hole injection by fixing one of the in-plane lattice constants while relaxing the other one. Figure S2 shows that Ti_2C MXene still possesses isotropic responses under a small amount of charge injection. As the hole injection increases, the 3-fold rotational symmetry breaks, which accounts for the emerging anisotropic actuation stresses of Ti_2C MXene in the armchair and zigzag directions (Figure S2). Upon hole injection of 0.13 e/atom, the actuation stress of Ti_2C MXene is 22.1 (25.4) GPa along the armchair (zigzag) direction, which is about 3 (6) times larger than that of BP.[48] Finally, our calculations demonstrated that the maximum actuation stresses of Ti_2C MXene along the armchair and zigzag directions can reach 31.1 and 25.7 GPa, respectively.

Afterward, gravimetric work density (W_g) of Ti_2C MXene upon hole injection was investigated as shown in Figure 3a.[15] Before that, the in-plane stiffness of Ti_2C MXene upon charge injection was first determined (Figure S3a). The in-plane stiffnesses of pristine Ti_2C MXene are 132.1 and 132.6 N/m along the armchair and zigzag directions, respectively, which agree with the values reported in the literature.[61,62] Considering the large in-plane isotropic actuation strain, W_g is calculated as the contribution from both armchair and zigzag directions (see Section 2 of the Supporting Information for details). As hole injection increases from 0.08 to 0.09 e/atom, W_g shows an abrupt increase from 97.8 to 780.3 J/g, mainly resulting from a large increase of actuation strain from 4.2 to

https://dx.doi.org/10.1021/acs.jpcc.0c09482
J. Phys. Chem. C 2021, 125, 1060−1068

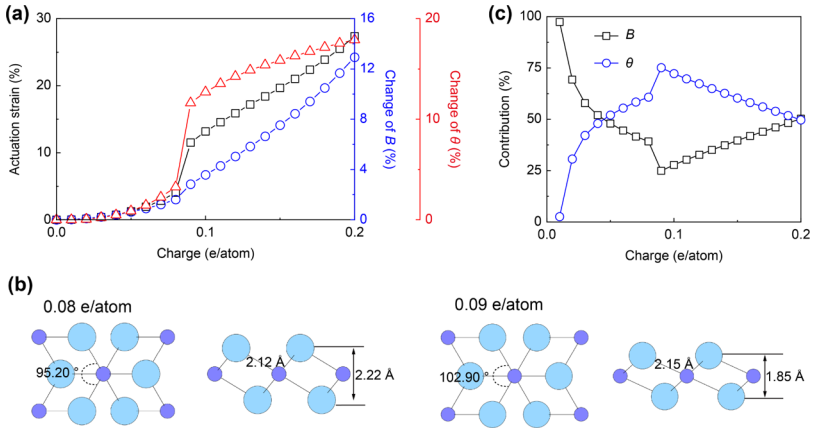

Figure 4. Actuation mechanism of Ti_2C MXene at atomic scale. (a) Actuation strain and changes of B and θ as a function of charge injection for Ti_2C MXene. (b) Atomistic structures of Ti_2C MXene upon hole injection of 0.08 and 0.09 e/atom, respectively. (c) Sensitivity analysis of B and θ on the actuation strain of Ti_2C MXene. Based on eq 2, the sensitivity analysis was implemented by substituting B (θ) and θ_0 (B_0) from the charged and pristine Ti_2C MXene into eq 2, respectively. The calculated actuation strain in this way is contributed by the change of B (θ), labeled as ε_B (ε_θ). The contributions from the changes of B and θ are defined as $\varepsilon_B/(\varepsilon_B + \varepsilon_\theta)$ and $\varepsilon_\theta/(\varepsilon_B + \varepsilon_\theta)$, respectively.

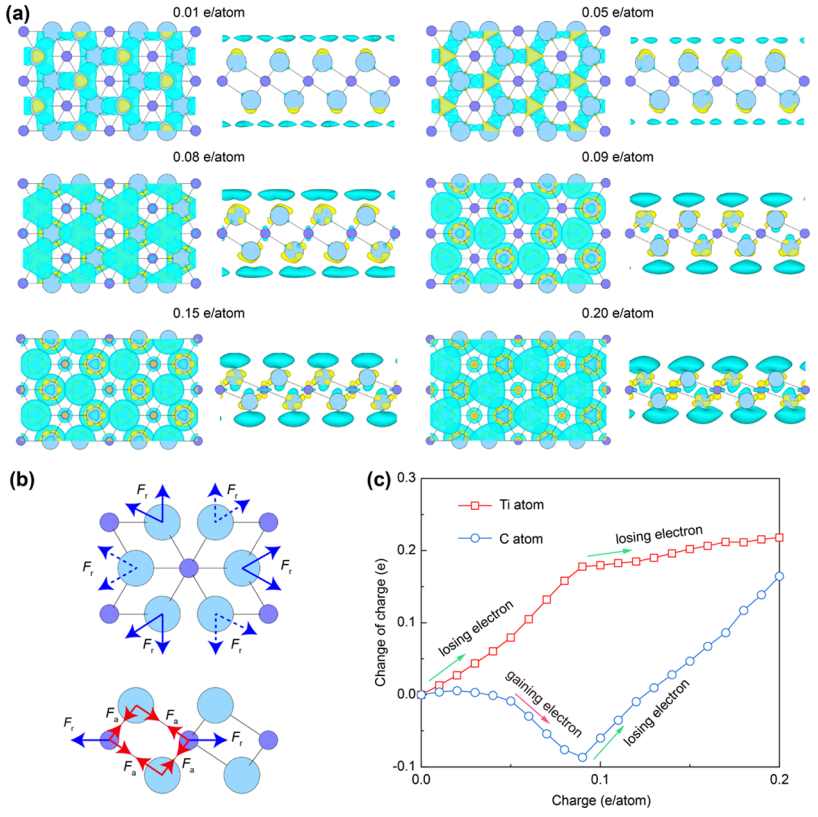

Figure 5. Actuation mechanism of Ti_2C MXene at electronic scale. (a) Excess charge density distribution of Ti_2C MXene upon hole injection of 0.01, 0.05, 0.08, 0.09, 0.15, and 0.20 e/atom with the iso-surface values of 0.00017, 0.00095, 0.0015, 0.0015, 0.002, and 0.002 e/Bohr^3, respectively. Colors of yellow and blue represent excess electrons and holes, respectively. (b) Illustration of the interatomic interactions including the repulsive force (F_r, blue arrows) and attractive force (F_a, red arrows) from the Coulombic interactions generated by the excess electron−electron (hole−hole) and electron−hole pairs, respectively. For the top view, the blue dashed arrows are labeled for Ti atoms at the top layer, and the blue solid arrows are labeled for Ti atoms at the bottom layer. (c) Change of Bader charge, defined as Bader charge for Ti and C atoms after hole injection subtracting their original values before hole injection, as a function of hole injection.

11.6%. Upon hole injection of 0.13 e/atom, W_g is determined to be 1725.2 J/g, which is higher than already-known 2D materials, such as silicene (23.1 J/g), BP (1076.2 J/g),[48] graphene (429.4 J/g, 0.15 e/atom), GO-C_4-sym-clamp (329.3 J/g), and GO-C_4-asym-unzip (1022.8 J/g).[42,43] With further hole injection, the maximum gravimetric work density (W_g) is 4360.2 J/g. Figure 3b compares the maximum areal actuation expansion and W_g of Ti_2C MXene with other 2D materials. Figure 3c shows the map of actuation strain and W_g of actuation materials, including traditional materials (e.g., piezoelectric ceramic and polymer), CNT-based yarns, metal rods, and 2D materials, which indicates that Ti_2C MXene has

https://dx.doi.org/10.1021/acs.jpcc.0c09482
J. Phys. Chem. C 2021, 125, 1060−1068

the combined properties of remarkable actuation strain, areal actuation expansion, and work density. Notably, since charge injection would change the in-plane stiffness,[48] we also calculated the work density based on the real in-plane stiffnesses of the charged Ti_2C MXene (Figure S3a), named as realistic work density (Figure S3b). The maximum realistic gravimetric work density ($W_{g\text{-}r}$) of Ti_2C MXene is as high as 1271.6 J/g (see Section 2 of the Supporting Information for details). Unless other noted, the realistic gravimetric work densities are reported in this work.

Mechanism for High Electromechanical Actuation Performance. To reveal the underlying mechanism for the high electromechanical actuation performance of Ti_2C MXene, we first took insight into the intrinsic structural changes by tracking the interatomic parameters of B and θ (Figure 1a). With the increase of hole injection, both B and θ increase (Figure 4a). The changes in B and θ of Ti_2C MXene upon hole injection are much larger than those upon electron injection, which agrees with the actuation responses upon electron and hole injection. Notably, with the increase of hole injection from 0.08 to 0.09 e/atom (Figure 4b), the bond length slightly increases from 2.12 to 2.15 Å, while the bond angle significantly increases from 95.20 to 102.90°, resulting in a large increase of actuation strain from 4.2 to 11.6%. Furthermore, Ti_2C MXene with a space group of $D_{3d}{}^3$ ($P\text{-}3m1$)[79] has 3-fold rotational symmetry (periodic rotational angle of 120°). On the basis of this rotational symmetry, the lattice constants of Ti_2C MXene can be derived as a function of interatomic parameters,

$$a = 2\sqrt{3}B\sin\frac{\theta}{2},\quad b = 2B\sin\frac{\theta}{2} \tag{1}$$

Then, the actuation strain (ε) of Ti_2C MXene in arbitrary direction is derived as

$$\varepsilon = \frac{B\sin(\theta/2)}{B_0\sin(\theta_0/2)} - 1 \tag{2}$$

where B_0 (B) and θ_0 (θ) are the bond length and bond angle before (after) charge injection. The atomic distance ($d_{Ti\text{-}Ti}$) can also be derived as

$$d_{Ti-Ti} = 2B\sqrt{1 - \frac{4}{3}\sin^2(\theta/2)} \tag{3}$$

Based on eqs 1 and 2 and first-principles calculations, the sensitivity analyses of B and θ were performed to determine their contributions on ε and $d_{Ti\text{-}Ti}$, respectively. As shown in Figure 4c, the actuation strain is first dominated by the change of bond length (B) under a small amount of hole injection (0.01−0.04 e/atom). With the increase of hole injection, θ begins to dominate the contribution (>50%) and then increases until a maximum contribution of 75.1% (hole injection of 0.09 e/atom). As the hole injection further increases from 0.10 to 0.20 e/atom, the contribution from B and θ increases and decreases to 50.3 and 49.7%, respectively. Similarly, the contribution of B and θ on $d_{Ti\text{-}Ti}$ was determined as shown in Figure S4a.

To further explore the origin of the extraordinary actuation performance of Ti_2C upon hole injection, we calculated the excess charge density from first-principles calculations (Figure 5a). Even upon hole injection of only 0.01 e/atom, both excessive holes and electrons emerge, indicating the redistribution of domestic valence electrons.[43,48] Most of the excess holes concentrate atop Ti atoms, while the excess electrons with a relatively low concentration are attached on Ti atoms (Figure 5a). As hole injection increases but below 0.09 e/atom, the excess charge distribution is similar with only a difference in the magnitude (Figure 5a), and very low excess holes attach atop C atoms aligned along the z direction (Figure S4b). Under the Coulomb interaction (Figure 5b), B and θ increase due to the repulsive interaction (F_r) resulting from the excess hole−hole and electron−electron pairs. Meanwhile, a weak attractive interaction (F_a) is expected to exist between Ti and C atoms resulting from the excess holes and electrons. Notably, as hole injection increases from 0.08 to 0.09 e/atom, the shapes of the excess holes around C atoms change from parallel to z direction to perpendicular to z direction (Figure S4c). The redistribution of excess holes around C atoms is expected to increase the repulsive interaction (F_r) between the neighboring C atoms, which helps to understand the significant increase of the distance between the neighboring C atoms from 3.14 to 3.36 Å. Additionally, we also provided the spd-projected density of states (PDOS) of Ti_2C MXene upon hole injection of 0, 0.05, 0.08, 0.09, 0.15, and 0.20 e/atom as shown in Figure S5. As the hole injection increases, the 3d-state of Ti atoms near the Fermi level (E_f = 0 eV) has a stronger local spike than that before hole injection. Notably, the hybridization between Ti 3d and C 2p is located in the range of −5 and −2 eV. The 2p states of C atoms change from high and low local spikes to be three low spikes as the hole injection increases from 0.08 to 0.09 e/atom, which is consistent with the changes of the excess charge density distributions of surrounding C atoms. Meanwhile, we found that the hybridization between Ti 3d and C 2p reaches a good overlap state at a hole injection of 0.09 e/atom, suggesting an improvement in the chemical bonding.

The excess charge analysis was further supported by Bader charge analysis[80] (Figure 5c). Because the electronegativity of C atoms is larger than that of Ti atoms, the electrons are transferred from Ti atoms to C atoms. Our calculations demonstrated that Ti and C atoms of Ti_2C MXene before charge injection lose and gain electrons of 1.066 and 2.132 per atom, respectively. Furthermore, the changes of the lost/gained electrons as a function of hole injection were calculated (Figure 5c). Upon hole injection of ≤0.03 e/atom, Bader charge analysis shows that the lost electrons of Ti atoms increase with the increase of hole injection, which contributes to the most depletion of electrons for Ti_2C MXene, while C atoms slightly lose electrons of only 0.003−0.006 electron per atom, agreeing with that the excess holes are mainly observed around Ti atoms and very little excess holes are atop C atoms (Figure 5a). As hole injection further increases (0.04−0.09 e/atom), Figure 5c shows that Ti atoms not only contribute to the depletion of electrons for Ti_2C MXene but also transfer more electrons to C atoms. Upon hole injection of >0.09 e/atom, C atoms stop to gain more electrons from Ti atoms and start to lose electrons. Notably, despite the increase of gained electrons of C atoms in this range of hole injection (0.04−0.09 e/atom), excess holes were still observed around C atoms because of the redistribution of valence electrons. As the gained electrons of C atoms increase, the electronegativity of C atoms would decrease. Hence, it is reasonable to expect that as the hole injection (the depletion of electron) increases, there will be a transition from gaining electrons to losing electrons for C atoms. Herein, the observed transition of hole injection is 0.09 e/atom (Figure 5c). In addition to the interaction

https://dx.doi.org/10.1021/acs.jpcc.0c09482
J. Phys. Chem. C 2021, 125, 1060−1068

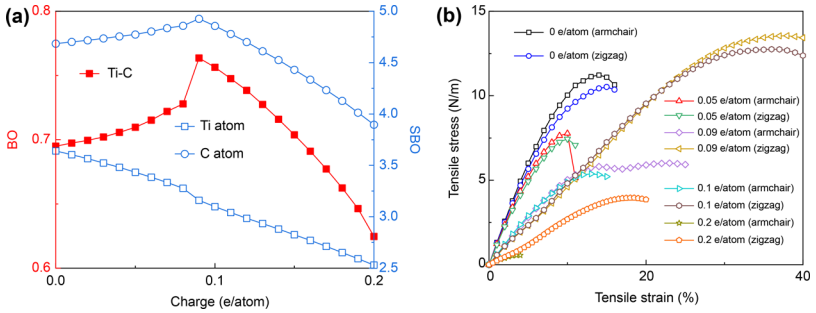

Figure 6. Structural integrity of charged Ti_2C MXene. (a) Bond order (BO) of Ti−C bonds and the sum of bond orders (SBOs) for Ti and C atoms, which were calculated using DDEC6 atomic population analysis.[81] (b) Mechanical tests show the structural integrity of Ti_2C MXene under a certain amount of electromechanical loads.

between excess charge, mechanical tests show that the in-plane stiffness of Ti_2C MXene significantly decreases with the increase of hole injection (Figure S3a), indicating that the increasing depletion of electrons (hole injection) significantly weakens Ti_2C MXene. Overall, the excess charge interaction and the softening of Ti_2C MXene upon hole injection jointly account for the high actuation performance of Ti_2C MXene.

Structural Integrity of Ti_2C MXene. The structural integrity of Ti_2C MXene under electromechanical loads plays a crucial role for practical applications. As mentioned above, our calculations demonstrated that the hole injection would reduce the in-plane stiffness (Figure S3a). The mechanical properties intrinsically result from the chemical bond features. Bond order (BO) is a measurement of the electron number involved in bonds between two atoms, which can be used as an indicator for measuring the chemical bond stability. Before hole injection, the BOs of different bonds (Ti−C, C−C, and Ti−Ti) were first determined (Figure S6), indicating that the dominant bonds are from the nearest Ti−C pairs because of the larger BOs than that of other bonds (C−C, Ti−Ti). The sum of BOs (SBOs) for C and Ti atoms is about 4.68 and 3.64, respectively (Figure 6a). Meanwhile, we examined the mechanical properties of Ti_2C upon hole injection. We first did uniaxial tensile tests for Ti_2C MXene (Figure 6b). The tensile strength of pristine Ti_2C MXene is 11.2 and 10.4 N/m along the armchair and zigzag directions, corresponding to the fracture strain of 14 and 15%, respectively. Then, uniaxial tensile tests of hole-injected Ti_2C MXene were conducted. Upon hole injection of 0.05, 0.09, 0.10, and 0.20 e/atom, the tensile strength along the armchair (zigzag) direction was calculated to be 7.8 (7.4), 6.0 (13.5), 5.4 (12.8), and 0.6 (4.0) N/m, corresponding to the fracture strain of 10% (10%), 23% (38%) 13% (36%), and 3.5% (18%), respectively. Notably, upon hole injection of 0.09 and 0.10 e/atom, Ti_2C MXene shows enhanced mechanical performance with a larger fracture strain than that of pristine Ti_2C MXene along the zigzag direction, which can be explained that BOs of Ti−C bonds reach their maximum values upon hole injection of 0.09 e/atom (Figure 6a). This abnormal phenomenon suggests that charge injection can be used as a strategy to enhance the strength and ductility of materials. Overall, our mechanical tests demonstrated that the structural integrity of Ti_2C MXene can be well maintained under a certain amount of electromechanical loads.

CONCLUSIONS

In summary, this work demonstrated the extraordinary electromechanical actuation performance of Ti_2C MXene. Ti_2C MXene shows a maximum actuation strain of 27.4% upon hole injection. Moreover, the large in-plane actuation strain is isotropic because of the 3-fold rotational symmetry, which results in the maximum areal actuation expansion of Ti_2C MXene (62.2%), larger than already-known 2D materials. Meanwhile, the maximum uniaxial and biaxial isometric actuation stresses and the maximum work density of Ti_2C MXene are also extraordinary. The underlying mechanism was explained through the analyses at atomic and electronic scales. Mechanical tests support that Ti_2C MXene can hold the structural integrity under a certain amount of electromechanical loads. Hence, Ti_2C MXene is attractive for applications of high-performance nanoactuators.

ASSOCIATED CONTENT

Supporting Information

The Supporting Information is available free of charge at https://pubs.acs.org/doi/10.1021/acs.jpcc.0c09482.

MXene upon hole injection (MP4)

Calculation details of actuation performance, mechanical properties and electronic structures of Ti_2C MXene upon charge injection, and summary of actuation performance of some typical actuation materials (PDF)

AUTHOR INFORMATION

Corresponding Author

Enlai Gao − *Department of Engineering Mechanics, School of Civil Engineering, Wuhan University, Wuhan, Hubei 430072, China;* orcid.org/0000-0003-1960-0260; Email: enlaigao@whu.edu.cn

Authors

Bozhao Wu − *Department of Engineering Mechanics, School of Civil Engineering, Wuhan University, Wuhan, Hubei 430072, China*

Xiaoxi Cai − *Department of Engineering Mechanics, School of Civil Engineering, Wuhan University, Wuhan, Hubei 430072, China*

Langquan Shui − *Department of Engineering Mechanics, School of Civil Engineering, Wuhan University, Wuhan, Hubei 430072, China;* orcid.org/0000-0002-5079-9629

Ze Liu − *Department of Engineering Mechanics, School of Civil Engineering, Wuhan University, Wuhan, Hubei 430072, China;* orcid.org/0000-0002-9906-5351

Complete contact information is available at: https://pubs.acs.org/10.1021/acs.jpcc.0c09482

Notes

The authors declare no competing financial interest.

■ ACKNOWLEDGMENTS

This work was supported by the National Natural Science Foundation of China (11902225), the Natural Science Foundation of Hubei Province (2019CFB174), and Wuhan Science and Technology Bureau (2019010701011390). The numerical calculations in this work have been done on the supercomputing system in the Supercomputing Center of Wuhan University.

■ REFERENCES

(1) Haines, C. S.; Lima, M. D.; Li, N.; Spinks, G. M.; Foroughi, J.; Madden, J. D. W.; Kim, S. H.; Fang, S.; Jung de Andrade, M.; Göktepe, F.; Göktepe, Ö.; Mirvakili, S. M.; Naficy, S.; Lepró, X.; Oh, J.; Kozlov, M. E.; Kim, S. J.; Xu, X.; Swedlove, B. J.; Wallace, G. G.; Baughman, R. H. Artificial Muscles from Fishing Line and Sewing Thread. *Science* **2014**, *343*, 868−872.

(2) Mirvakili, S. M.; Hunter, I. W. Multidirectional Artificial Muscles from Nylon. *Adv. Mater.* **2017**, *29*, No. 1604734.

(3) Jiang, T. Y.; Ng, T. Y.; Lam, K. Y. Optimization of a Piezoelectric Ceramic Actuator. *Sens. Actuators, A* **2000**, *84*, 81−94.

(4) Hathaway, K. B.; Clark, A. E. Magnetostrictive Materials. *MRS Bull.* **1993**, *18*, 34−41.

(5) Kim, K. H.; Yoon, H. J.; Jeong, O. C.; Yang, S. S. Fabrication and Test of a Micro Electromagnetic Actuator. *Sens. Actuators, A* **2005**, *117*, 8−16.

(6) Megregany, M.; Nagarkar, P.; Senturia, S. D.; Lang, J. H. In *Operation of MicrofabricatedHarmonic and Ordinary Side-Drive Motors*, EEE Proceedings on Micro Electro Mechanical Systems, An Investigation of Micro Structures, Sensors, Actuators, Machinesand Robots; IEEE, 1990; pp 1−8.

(7) Fennimore, A.; Yuzvinsky, T.; Han, W.-Q.; Fuhrer, M.; Cumings, J.; Zettl, A. Rotational Actuators Based on Carbon Nanotubes. *Nature* **2003**, *424*, 408−410.

(8) King, T. G.; Preston, M. E.; Murphy, B. J. M.; Cannell, D. S. Piezoelectric Ceramic Actuators: A Review of Machinery Applications. *Precis. Eng.* **1990**, *12*, 131−136.

(9) Baughman, R. H. Conducting Polymers in Redox Devices and Intelligent Materials Systems. *Makromol. Chem., Macromol. Symp.* **1991**, *51*, 193−215.

(10) Baughman, R. H.; Shacklette, L. W.; Elsenbaumer, R. L.; Plichta, E. J.; Becht, C. Micro Electromechanical Actuators Based on Conducting Polymers. In *Molecular Electronics: Materials and Methods*; Lazarev, P. I., Ed.; Springer Netherlands: Dordrecht, 1991; pp 267−289.

(11) Shakuda, S.; Morita, S.; Kawai, T.; Yoshino, K. Dynamic Characteristics of Bimorph with Conducting Polymer Gel. *Jpn. J. Appl. Phys.* **1993**, *32*, 5143−5146.

(12) Zhenyi, M.; Scheinbeim, J. I.; Lee, J. W.; Newman, B. A. High Field Electrostrictive Response of Polymers. *J. Polym. Sci., Part B: Polym. Phys.* **1994**, *32*, 2721−2731.

(13) Baughman, R. H. Conducting Polymer Artificial Muscles. *Synth. Met.* **1996**, *78*, 339−353.

(14) Park, S.-E.; Shrout, T. R. Ultrahigh Strain and Piezoelectric Behavior in Relaxor Based Ferroelectric Single Crystals. *J. Appl. Phys.* **1997**, *82*, 1804−1811.

(15) Baughman, R. H. Carbon Nanotube Actuators. *Science* **1999**, *284*, 1340−1344.

(16) Mirvakili, S. M.; Hunter, I. W. Artificial Muscles: Mechanisms, Applications, and Challenges. *Adv. Mater.* **2018**, *30*, No. 1704407.

(17) Mirvakili, S. M.; Pazukha, A.; Sikkema, W.; Sinclair, C. W.; Spinks, G. M.; Baughman, R. H.; Madden, J. D. Niobium Nanowire Yarns and Their Application as Artificial Muscles. *Adv. Funct. Mater.* **2013**, *23*, 4311−4316.

(18) Duduta, M.; Hajiesmaili, E.; Zhao, H.; Wood, R. J.; Clarke, D. R. Realizing the Potential of Dielectric Elastomer Artificial Muscles. *Proc. Natl. Acad. Sci. U.S.A* **2019**, *116*, 2476−2481.

(19) Mu, J.; Jung de Andrade, M.; Fang, S.; Wang, X.; Gao, E.; Li, N.; Kim, S. H.; Wang, H.; Hou, C.; Zhang, Q.; Zhu, M.; Qian, D.; Lu, H.; Kongahage, D.; Talebian, S.; Foroughi, J.; Spinks, G.; Kim, H.; Ware, T. H.; Sim, H. J.; Lee, D. Y.; Jang, Y.; Kim, S. J.; Baughman, R. H. Sheath-Run Artificial Muscles. *Science* **2019**, *365*, 150−155.

(20) Hollerbach J M, H. I. W.; Ballantyne, J. A Comparative Analysis of Actuator Technologies for Robotics. *Rob. Rev.* **1992**, *2*, 299−342.

(21) Lv, S.; Dudek, D. M.; Cao, Y.; Balamurali, M. M.; Gosline, J.; Li, H. Designed Biomaterials to Mimic the Mechanical Properties of Muscles. *Nature* **2010**, *465*, 69−73.

(22) Winzeler-Merçay, U.; Mudie, H. The Nature of the Effects of Stroke on Trunk Flexor and Extensor Muscles During Work and at Rest. *Disabil. Rehabil.* **2002**, *24*, 875−886.

(23) Madden, J. D. W.; Vandesteeg, N. A.; Anquetil, P. A.; Madden, P. G. A.; Takshi, A.; Pytel, R. Z.; Lafontaine, S. R.; Wieringa, P. A.; Hunter, I. W. Artificial Muscle Technology: Physical Principles and Naval Prospects. *IEEE J. Oceanic Eng.* **2004**, *29*, 706−728.

(24) Heo, S.; Kim, Y. Y. Optimal Design and Fabrication of Mems Rotary Thermal Actuators. *J. Micromech. Microeng.* **2007**, *17*, 2241−2247.

(25) Lai, H.-Y.; Hsu, C.-H.; Chen, C.-K. Optimal Design and System Characterization of Graphene Sheets in a Micro/Nano Actuator. *Comput. Mater. Sci.* **2016**, *117*, 478−488.

(26) Miskin, M. Z.; Cortese, A. J.; Dorsey, K.; Esposito, E. P.; Reynolds, M. F.; Liu, Q.; Cao, M.; Muller, D. A.; McEuen, P. L.; Cohen, I. Electronically Integrated, Mass-Manufactured, Microscopic Robots. *Nature* **2020**, *584*, 557−561.

(27) Aliev, A. E.; Oh, J.; Kozlov, M. E.; Kuznetsov, A. A.; Fang, S.; Fonseca, A. F.; Ovalle, R.; Lima, M. D.; Haque, M. H.; Gartstein, Y. N.; et al. Giant-Stroke, Superelastic Carbon Nanotube Aerogel Muscles. *Science* **2009**, *323*, 1575−1578.

(28) Hyeon, J. S.; Park, J. W.; Baughman, R. H.; Kim, S. J. Electrochemical Graphene/Carbon Nanotube Yarn Artificial Muscles. *Sens. Actuators, B* **2019**, *286*, 237−242.

(29) Qiao, J.; Di, J.; Zhou, S.; Jin, K.; Zeng, S.; Li, N.; Fang, S.; Song, Y.; Li, M.; Baughman, R. H.; Li, Q. Large-Stroke Electrochemical Carbon Nanotube/Graphene Hybrid Yarn Muscles. *Small* **2018**, *14*, No. 1801883.

(30) Sun, G.; Kertesz, M.; Kürti, J.; Baughman, R. H. Dimensional Change as a Function of Charge Injection in Graphite Intercalation Compounds: A Density Functional Theory Study. *Phys. Rev. B* **2003**, *68*, No. 125411.

(31) Sun, G.; Kürti, J.; Kertesz, M.; Baughman, R. H. Dimensional Changes as a Function of Charge Injection in Single-Walled Carbon Nanotubes. *J. Am. Chem. Soc.* **2002**, *124*, 15076−15080.

(32) Liu, J. Z.; Hughes, J. Electromechanical Actuation of Pristine Graphene and Graphene Oxide: Origin, Optimization, and Comparison 2019, arXiv:1903.02729. arXiv.org e-Print archive. https://arxiv.org/abs/1903.02729.

(33) Van Thanh, V.; Hung, N. T.; Van Truong, D. Charge-Induced Electromechanical Actuation of Mo- and W-Dichalcogenide Monolayers. *RSC Adv.* **2018**, *8*, 38667−38672.

(34) Chen, K.; Deng, J.; Shi, Q.; Ding, X.; Sun, J.; Yang, S.; Liu, J. Z. Charge Doping Induced Reversible Multistep Structural Phase Transitions and Electromechanical Actuation in Two-Dimensional 1T-MoS_2. *Nanoscale* **2020**, *12*, 12541−12550.

(35) Sun, S.; Zuo, H.; Zhang, T.-Y. Joint First-Principles/Continuum Calculations of Electromechanical Properties of MoS2 Monolayer. *Appl. Phys. Lett.* **2014**, *105*, No. 061910.

(36) Lu, L.; Liu, J.; Hu, Y.; Chen, W. Large Volume Variation of an Anisotropic Graphene Nanosheet Electrochemical-Mechanical Actuator Under Low Voltage Stimulation. *Chem. Commun.* **2012**, *48*, 3978−3980.

(37) Liang, J.; Huang, Y.; Oh, J.; Kozlov, M.; Sui, D.; Fang, S.; Baughman, R. H.; Ma, Y.; Chen, Y. Electromechanical Actuators

https://dx.doi.org/10.1021/acs.jpcc.0c09482
J. Phys. Chem. C 2021, 125, 1060−1068

Based on Graphene and Graphene/Fe_3O_4 Hybrid Paper. *Adv. Funct. Mater.* **2011**, *21*, 3778−3784.
(38) Xie, X.; Qu, L.; Zhou, C.; Li, Y.; Zhu, J.; Bai, H.; Shi, G.; Dai, L. An Asymmetrically Surface-Modified Graphene Film Electrochemical Actuator. *ACS Nano* **2010**, *4*, 6050−6054.
(39) Liu, J.; Wang, Z.; Xie, X.; Cheng, H.; Zhao, Y.; Qu, L. A Rationally-Designed Synergetic Polypyrrole/Graphene Bilayer Actuator. *J. Mater. Chem.* **2012**, *22*, 4015−4020.
(40) Liu, J.; Wang, Z.; Zhao, Y.; Cheng, H.; Hu, C.; Jiang, L.; Qu, L. Three-Dimensional Graphene-Polypyrrole Hybrid Electrochemical Actuator. *Nanoscale* **2012**, *4*, 7563−7568.
(41) Sun, S.; Zhang, T.-Y. Charge- and Thickness-Dependent Inplane Deformation of Multilayer Graphene Thin Films. *Phys. Chem. Chem. Phys.* **2016**, *18*, 3694−3699.
(42) Rogers, G. W.; Liu, J. Z. High-Performance Graphene Oxide Electromechanical Actuators. *J. Am. Chem. Soc.* **2012**, *134*, 1250−1255.
(43) Rogers, G. W.; Liu, J. Z. Monolayer Graphene Oxide as a Building Block for Artificial Muscles. *Appl. Phys. Lett.* **2013**, *102*, No. 021903.
(44) Chang, Z.; Yan, W.; Shang, J.; Liu, J. Z. Piezoelectric Properties of Graphene Oxide: A First-Principles Computational Study. *Appl. Phys. Lett.* **2014**, *105*, No. 023103.
(45) Chang, Z.; Deng, J.; Chandrakumara, G. G.; Yan, W.; Liu, J. Z. Two-Way Actuation of Graphene Oxide Arising from Quantum Mechanical Effects. *Appl. Phys. Lett.* **2016**, *109*, No. 143902.
(46) Chang, Z.; Deng, J.; Chandrakumara, G. G.; Yan, W.; Liu, J. Z. Two-Dimensional Shape Memory Graphene Oxide. *Nat. Commun.* **2016**, *7*, No. 11972.
(47) Rogers, G. W.; Liu, J. Z. Graphene Actuators: Quantum-Mechanical and Electrostatic Double-Layer Effects. *J. Am. Chem. Soc.* **2011**, *133*, 10858−10863.
(48) Wu, B.; Deng, H.-X.; Jia, X.; Shui, L.; Gao, E.; Liu, Z. High-Performance Phosphorene Electromechanical Actuators. *npj Comput. Mater.* **2020**, *6*, No. 27.
(49) Naguib, M.; Kurtoglu, M.; Presser, V.; Lu, J.; Niu, J.; Heon, M.; Hultman, L.; Gogotsi, Y.; Barsoum, M. W. Two-Dimensional Nanocrystals Produced by Exfoliation of Ti_3AlC_2. *Adv. Mater.* **2011**, *23*, 4248−4253.
(50) Naguib, M.; Mashtalir, O.; Carle, J.; Presser, V.; Lu, J.; Hultman, L.; Gogotsi, Y.; Barsoum, M. W. Two-Dimensional Transition Metal Carbides. *ACS Nano* **2012**, *6*, 1322−1331.
(51) Lukatskaya, M. R.; Mashtalir, O.; Ren, C. E.; Dall'Agnese, Y.; Rozier, P.; Taberna, P. L.; Naguib, M.; Simon, P.; Barsoum, M. W.; Gogotsi, Y. Cation Intercalation and High Volumetric Capacitance of Two-Dimensional Titanium Carbide. *Science* **2013**, *341*, 1502−1505.
(52) Khazaei, M.; Arai, M.; Sasaki, T.; Estili, M.; Sakka, Y. Two-Dimensional Molybdenum Carbides: Potential Thermoelectric Materials of the Mxene Family. *Phys. Chem. Chem. Phys.* **2014**, *16*, 7841−7849.
(53) Liu, F.; Zhou, A.; Chen, J.; Zhang, H.; Cao, J.; Wang, L.; Hu, Q. Preparation and Methane Adsorption of Two-Dimensional Carbide Ti_2C. *Adsorption* **2016**, *22*, 915−922.
(54) Zhang, X.; Xu, J.; Wang, H.; Zhang, J.; Yan, H.; Pan, B.; Zhou, J.; Xie, Y. Ultrathin Nanosheets of Max Phases with Enhanced Thermal and Mechanical Properties in Polymeric Compositions: $Ti_3Si_{0.75}Al_{0.25}C_2$. *Angew. Chem.* **2013**, *125*, 4457−4461.
(55) Xue, M.; Wang, Z.; Yuan, F.; Zhang, X.; Wei, W.; Tang, H.; Li, C. Preparation of $TiO_2/Ti_3C_2T_x$ Hybrid Nanocomposites and Their Tribological Properties as Base Oil Lubricant Additives. *RSC Adv.* **2017**, *7*, 4312−4319.
(56) Ling, Z.; Ren, C. E.; Zhao, M.-Q.; Yang, J.; Giammarco, J. M.; Qiu, J.; Barsoum, M. W.; Gogotsi, Y. Flexible and Conductive Mxene Films and Nanocomposites with High Capacitance. *Proc. Natl. Acad. Sci. U.S.A.* **2014**, *111*, 16676.
(57) Peng, Q.; Guo, J.; Zhang, Q.; Xiang, J.; Liu, B.; Zhou, A.; Liu, R.; Tian, Y. Unique Lead Adsorption Behavior of Activated Hydroxyl Group in Two-Dimensional Titanium Carbide. *J. Am. Chem. Soc.* **2014**, *136*, 4113−4116.
(58) Seh, Z. W.; Fredrickson, K. D.; Anasori, B.; Kibsgaard, J.; Strickler, A. L.; Lukatskaya, M. R.; Gogotsi, Y.; Jaramillo, T. F.; Vojvodic, A. Two-Dimensional Molybdenum Carbide (Mxene) as an Efficient Electrocatalyst for Hydrogen Evolution. *ACS Energy Letters* **2016**, *1*, 589−594.
(59) Lin, H.; Wang, X.; Yu, L.; Chen, Y.; Shi, J. Two-Dimensional Ultrathin Mxene Ceramic Nanosheets for Photothermal Conversion. *Nano Lett.* **2017**, *17*, 384−391.
(60) Gogotsi, Y.; Anasori, B. The Rise of Mxenes. *ACS Nano* **2019**, *13*, 8491−8494.
(61) Wang, S.; Li, J.-X.; Du, Y.-L.; Cui, C. First-Principles Study on Structural, Electronic and Elastic Properties of Graphene-Like Hexagonal Ti_2C Monolayer. *Comput. Mater. Sci.* **2014**, *83*, 290−293.
(62) Borysiuk, V.; Mochalin, V.; Gogotsi, Y. In *Molecular Dynamics Study of the MechanicalProperties of the Grapheme-Like Titanium Carbide Ti_2SC*, Proceedings of the International Conference Nanomaterials: Applications and Properties; Sumy State University Publishing, 2014; pp 01CBNM02.
(63) Chakraborty, P.; Das, T.; Nafday, D.; Boeri, L.; Saha-Dasgupta, T. Manipulating the Mechanical Properties of Ti_2C Mxene: Effect of Substitutional Doping. *Phys. Rev. B* **2017**, *95*, No. 184106.
(64) Zhang, H.; Fu, Z.; Zhang, R.; Zhang, Q.; Tian, H.; Legut, D.; Germann, T. C.; Guo, Y.; Du, S.; Francisco, J. S. Designing Flexible 2D Transition Metal Carbides with Strain-Controllable Lithium Storage. *Proc. Natl. Acad. Sci. U.S.A.* **2017**, *114*, E11082−E11091.
(65) Come, J.; Black, J. M.; Lukatskaya, M. R.; Naguib, M.; Beidaghi, M.; Rondinone, A. J.; Kalinin, S. V.; Wesolowski, D. J.; Gogotsi, Y.; Balke, N. Controlling the Actuation Properties of Mxene Paper Electrodes Upon Cation Intercalation. *Nano Energy* **2015**, *17*, 27−35.
(66) Pang, D.; Alhabeb, M.; Mu, X.; Dall'Agnese, Y.; Gogotsi, Y.; Gao, Y. Electrochemical Actuators Based on Two-Dimensional Ti_3CT_x (Mxene). *Nano Lett.* **2019**, *19*, 7443−7448.
(67) Umrao, S.; Tabassian, R.; Kim, J.; Nguyen, V. H.; Zhou, Q.; Nam, S.; Oh, I.-K. Mxene Artificial Muscles Based on Ionically Cross-Linked $Ti_3C_2T_x$ Electrode for Kinetic Soft Robotics. *Sci. Rob.* **2019**, *4*, No. eaaw7797.
(68) Cao, J.; Zhou, Z.; Song, Q.; Chen, K.; Su, G.; Zhou, T.; Zheng, Z.; Lu, C.; Zhang, X. Ultrarobust $Ti_3C_2T_x$ Mxene-Based Soft Actuators via Bamboo-Inspired Mesoscale Assembly of Hybrid Nanostructures. *ACS Nano* **2020**, *14*, 7055−7065.
(69) Kresse, G.; Furthmüller, J. Efficient Iterative Schemes for Ab Initio Total-Energy Calculations Using a Plane-Wave Basis Set. *Phys. Rev. B.* **1996**, *54*, 11169.
(70) Kresse, G.; Furthmüller, J. Efficiency of Ab-Initio Total Energy Calculations for Metals and Semiconductors Using a Plane-Wave Basis Set. *Comput. Mater. Sci.* **1996**, *6*, 15−50.
(71) Perdew, J. P.; Burke, K.; Ernzerhof, M. Generalized Gradient Approximation Made Simple. *Phys. Rev. Lett.* **1996**, *77*, 3865−3868.
(72) Filippi, C.; Singh, D. J.; Umrigar, C. All-Electron Local-Density and Generalized-Gradient Calculations of the Structural Properties of Semiconductors. *Phys. Rev. B* **1994**, *50*, 14947.
(73) Grimme, S.; Antony, J.; Ehrlich, S.; Krieg, H. A Consistent and Accurate Ab Initio Parametrization of Density Functional Dispersion Correction (DFT-D) for the 94 Elements H-Pu. *J. Chem. Phys.* **2010**, *132*, No. 154104.
(74) Monkhorst, H. J.; Pack, J. D. Special Points for Brillouin-Zone Integrations. *Phys. Rev. B* **1976**, *13*, 5188−5192.
(75) Bian, W.; Zhao, J.; You, Z. Low Voltage, High Speed and Small Area In-Plane Mems Switch. *J. Micromech. Microeng.* **2019**, *29*, No. 065014.
(76) Hafiz, M. A. A.; Kosuru, L.; Ramini, A.; Chappanda, K. N.; Younis, M. I. In-Plane Mems Shallow Arch Beam for Mechanical Memory. *Micromachines* **2016**, *7*, 191.
(77) de Oliveira Hansen, R.; Mátéfi-Tempfli, M.; Safonovs, R.; Adam, J.; Chemnitz, S.; Reimer, T.; Wagner, B.; Benecke, W.; Mátéfi-Tempfli, S. Magnetic Films for Electromagnetic Actuation in Mems Switches. *Microsyst. Technol.* **2018**, *24*, 1987−1994.

https://dx.doi.org/10.1021/acs.jpcc.0c09482
J. Phys. Chem. C 2021, 125, 1060−1068

(78) Weibel, D. B.; Kruithof, M.; Potenta, S.; Sia, S. K.; Lee, A.; Whitesides, G. M. Torque-Actuated Valves for Microfluidics. *Anal. Chem.* **2005**, *77*, 4726−4733.
(79) Fredrickson, K. D.; Anasori, B.; Seh, Z. W.; Gogotsi, Y.; Vojvodic, A. Effects of Applied Potential and Water Intercalation on the Surface Chemistry of Ti_2C and Mo_2C Mxenes. *J. Phys. Chem. C* **2016**, *120*, 28432−28440.
(80) Henkelman, G.; Arnaldsson, A.; Jónsson, H. A Fast and Robust Algorithm for Bader Decomposition of Charge Density. *Comput. Mater. Sci.* **2006**, *36*, 354−360.
(81) Manz, T. A. Introducing DDEC6 Atomic Population Analysis: Part 3. Comprehensive Method to Compute Bond Orders. *RSC Adv.* **2017**, *7*, 45552−45581.

https://dx.doi.org/10.1021/acs.jpcc.0c09482
J. Phys. Chem. C 2021, 125, 1060−1068

Supporting information

Extraordinary Electromechanical Actuation of Ti_2C MXene

Bozhao Wu, Xiaoxi Cai, Langquan Shui, Enlai Gao* and Ze Liu

Department of Engineering Mechanics, School of Civil Engineering, Wuhan University, Wuhan, Hubei 430072, China.

*Corresponding author. E-mail: enlaigao@whu.edu.cn

This supporting information contains

(1) Sections 1-2.

(2) Figures S1-S6.

(3) Table S1.

(4) Movie S1.

Section 1: Calculations of actuation performance

(1) Actuation strain

The actuation strain of Ti_2C MXene upon charge injection along the armchair (*x* direction) or zigzag (*y* direction) direction is defined as:

$$\varepsilon_x = \frac{a - a_0}{a_0}, \varepsilon_y = \frac{b - b_0}{b_0} \quad (1)$$

where a_0 and b_0 are lattice constants of pristine Ti_2C MXene, a and b are the lattice constants of Ti_2C MXene upon charge injection, respectively. Figure 2a shows the actuation strain of Ti_2C MXene upon charge injection as compared with other 2D materials (Figure S1a).

(2) Areal actuation expansion

As shown in Figure 2a, the charged Ti_2C MXene shows the same actuation strain along the armchair and zigzag directions. The areal actuation expansion (S_ε) of the charged Ti_2C MXene is characterized by the following formula:

$$S_\varepsilon = \frac{ab - a_0 b_0}{a_0 b_0} \quad (2)$$

Eq. (2) can be rewritten as:

$$S_\varepsilon = (\varepsilon_x + 1)(\varepsilon_y + 1) - 1 \quad (3)$$

The calculated S_ε was shown in Figure 2a. Besides, according to the data in Figure S1a, the areal actuation expansions of graphene, silicene and black phosphorene (BP) were also determined for the comparison with that of Ti_2C monolayer (Figure S1b).

Section 2: Calculation of gravimetric work densities

The gravimetric work densities (W_g) for 2D materials are usually defined as[1]:

$$W_g = \frac{S\varepsilon_{max}^2}{2\rho} \tag{4}$$

where ε_{max} is the maximum actuation strain upon charge injection, S is the in-plane stiffness and ρ is the areal density of 2D materials. Considering the significant actuation strain both along the zigzag and armchair directions of Ti_2C MXene, the total gravimetric work density should be contributed from both armchair and zigzag directions:

$$W_{vol} = W_{g,\,armchair} + W_{g,\,zigzag} \tag{5}$$

Additionally, previous work demonstrated that the in-plane stiffness of charged phosphorene would remarkably reduce upon hole injection[2]. As shown in Figure S3a, the in-plane stiffnesses of hole charged Ti_2C monolayer also show a reduction with the increase of hole injection. To address this issue, a realistic gravimetric work density ($W_{g\text{-}r}$) is defined as[2]

$$W_{g\text{-}r} = \frac{1}{2\rho}\int \sigma_i d\varepsilon_i \tag{6}$$

The total realistic gravimetric work densities are written as

$$W_{g\text{-}r} = W_{g\text{-}r,\,armchair} + W_{g\text{-}r,\,zigzag} \tag{7}$$

The calculated realistic work densities ($W_{g\text{-}r}$) are shown in Figure S3b.

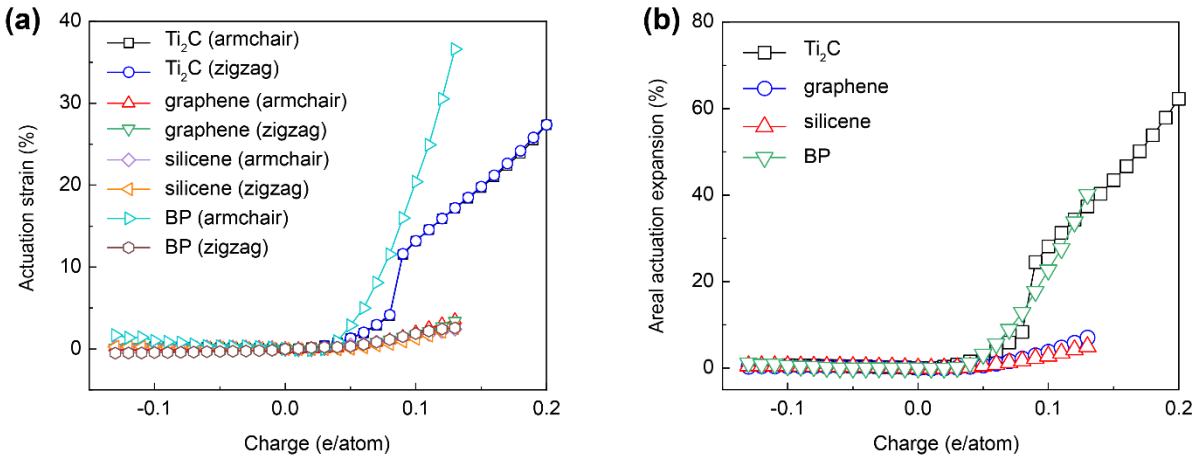

Figure S1. (a) Actuation strain and (b) areal actuation expansion of Ti_2C MXene upon charge injection, as compared with graphene, silicene and black phosphorene (BP) monolayer. The data of graphene, silicene and BP was adopted from the **Ref**[2].

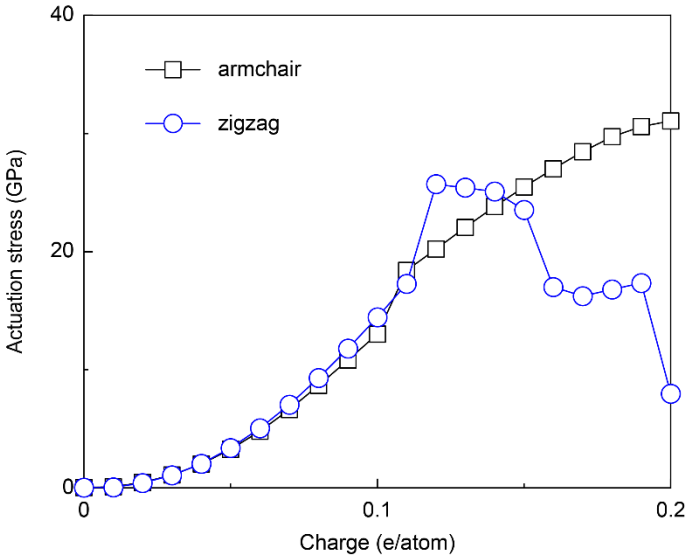

Figure S2. Uniaxial actuation stress of Ti_2C MXene upon charge injection.

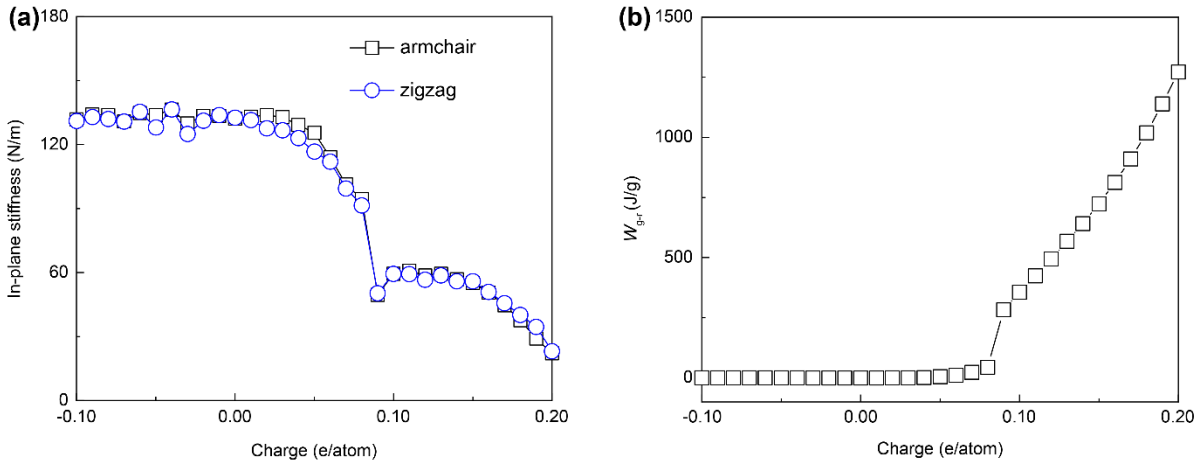

Figure S3. (a) In-plane stiffnesses of the charged Ti_2C MXene along the armchair and zigzag directions. (b) Realistic gravimetric work densities ($W_{g\text{-}r}$) of Ti_2C MXene.

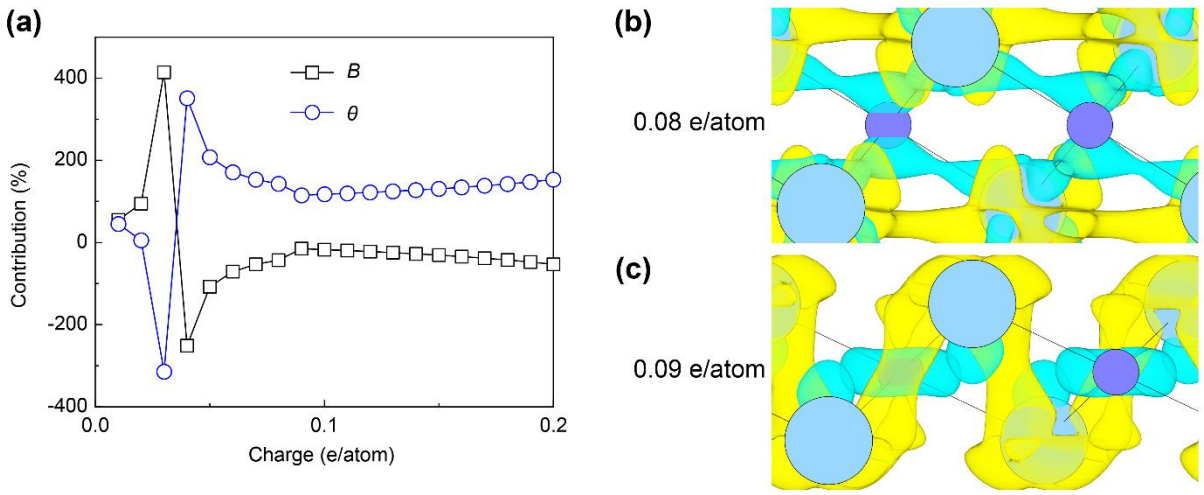

Figure S4. (a) Contributions of internal bond (B) and bond angle (θ) on the interlayer thickness ($d_{Ti\text{-}Ti}$) for Ti_2C MXene. The partial zoom of the excess charge density distributions of Ti_2C MXene upon (b) 0.08 and (c) 0.09 e/atom injection with an iso-surface value of 0.0005 e/Bohr^3.

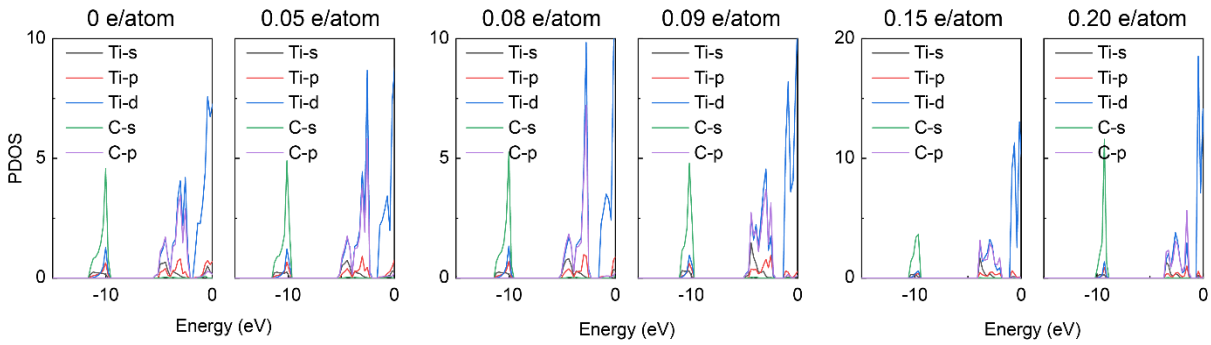

Figure S5. Projected density of state (PDOS) of the charged Ti_2C MXene upon hole injection of 0.05, 0.08, 0.09, 0.15 and 0.20 e/atom as compared with pristine Ti_2C MXene.

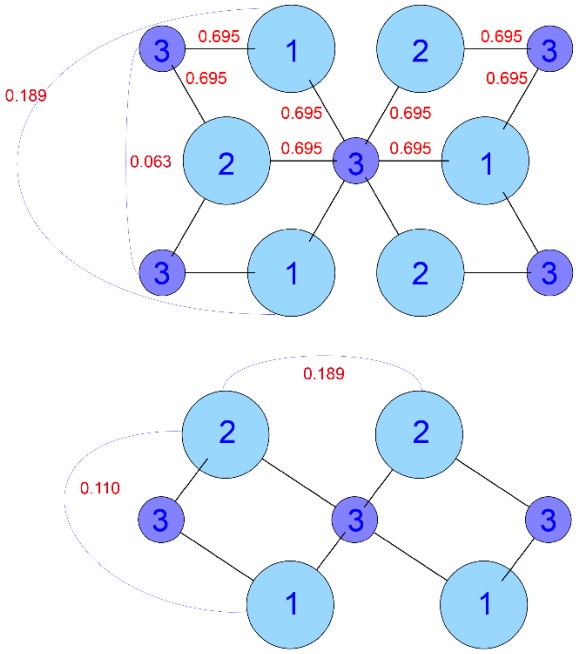

Figure S6. Bond orders (BOs) for different bond pairs (Ti-C, C-C and Ti-Ti) of the pristine Ti_2C MXene calculated by using DDEC6 atomic population analysis[3].

Table S1 Summary of maximum actuation strain ε_{max} (%) and gravimetric work density W_g (J/g) of typical actuation materials.

Type	Materials name	ε_{max}	W_g
Traditional materials	Natural muscle[4]	40	0.0386
	Magnetostrictor[5]	0.2	0.0216
	PZN-PT single crystal[6]	1.7	0.131
	Polyurethane elastomer[7]	4	0.013
	P(VDF-TrFE)[8]	4	0.16
	Polyaniline yarn[9]	0.28	0.0056
Metal	Pd rod[10]	3.3	1.27
	Au-Pt alloy rod[11]	1.3	0.4
2D materials	CNT aerogel sheets[12]	1.5	0.03
	CNT buckypaper[1]	1	24
	Coiled graphene/CNT yarn[13]	19.4	2.6
	Coiled CNT/rGO yarn[14]	8.1	0.236
	CNT@nylon6 SRAM[15]	4.7	0.99
	Two-ply coiled CNT yarn[16]	16.5	2.2
	GO-C_4O-asym-unzip[17]	9.6	1022.8
	GO-C_4O-sym-clamp[18]	6.3	329.3
	1H-WTe_2[19]	2.9	18.6
	Silicene[2]	2.5	23.1
	Graphene[2, 18] 0.13 (0.15) e/atom	3.5 (4.7)	280.2 (429.4)
	Phosphorene[2]	36.6	1076.2
	Ti_2C MXene	27.4	4360.2

Movie S1

Structure changes of Ti_2C MXene upon hole injection from 0.00 to 0.20 e/atom from the top and side views.

References

1. Baughman, R. H., Carbon nanotube actuators. *Science* **1999,** *284* (5418), 1340-1344.
2. Wu, B.; Deng, H.-X.; Jia, X.; Shui, L.; Gao, E.; Liu, Z., High-performance phosphorene electromechanical actuators. *npj Computational Materials* **2020,** *6* (1), 27.
3. Manz, T. A., Introducing DDEC6 atomic population analysis: part 3. Comprehensive method to compute bond orders. *RSC Advances* **2017,** *7* (72), 45552-45581.
4. Madden, J. D. W.; Vandesteeg, N. A.; Anquetil, P. A.; Madden, P. G. A.; Takshi, A.; Pytel, R. Z.; Lafontaine, S. R.; Wieringa, P. A.; Hunter, I. W., Artificial muscle technology: Physical principles and naval prospects. *IEEE Journal of Oceanic Engineering* **2004,** *29* (3), 706-728.
5. Hathaway, K. B.; Clark, A. E., Magnetostrictive materials. *MRS Bulletin* **1993,** *18* (4), 34-41.
6. Park, S.-E.; Shrout, T. R., Ultrahigh strain and piezoelectric behavior in relaxor based ferroelectric single crystals. *Journal of Applied Physics* **1997,** *82* (4), 1804-1811.
7. Zhenyi, M.; Scheinbeim, J. I.; Lee, J. W.; Newman, B. A., High field electrostrictive response of polymers. *Journal of Polymer Science Part B: Polymer Physics* **1994,** *32* (16), 2721-2731.
8. Zhang, Q. M.; Bharti, V.; Zhao, X., Giant electrostriction and relaxor ferroelectric behavior in electron-irradiated poly(vinylidene fluoride-trifluoroethylene) copolymer. *Science* **1998,** *280* (5372), 2101-2104.
9. Lu, W.; Fadeev, A. G.; Qi, B.; Smela, E.; Mattes, B. R.; Ding, J.; Spinks, G. M.; Mazurkiewicz, J.; Zhou, D.; Wallace, G. G.; MacFarlane, D. R.; Forsyth, S. A.; Forsyth, M., Use of ionic liquids for π-conjugated polymer electrochemical devices. *Science* **2002,** *297* (5583), 983.
10. Zhang, J.; Bai, Q.; Zhang, Z., Dealloying-driven nanoporous palladium with superior electrochemical actuation performance. *Nanoscale* **2016,** *8* (13), 7287-7295.
11. Jin, H.-J.; Wang, X.-L.; Parida, S.; Wang, K.; Seo, M.; Weissmüller, J., Nanoporous Au−Pt Alloys As Large Strain Electrochemical Actuators. *Nano Letters* **2010,** *10* (1), 187-194.
12. Aliev, A. E.; Oh, J.; Kozlov, M. E.; Kuznetsov, A. A.; Fang, S.; Fonseca, A. F.; Ovalle, R.; Lima, M. D.; Haque, M. H.; Gartstein, Y. N., Giant-stroke, superelastic carbon nanotube aerogel muscles. *Science* **2009,** *323* (5921), 1575-1578.
13. Hyeon, J. S.; Park, J. W.; Baughman, R. H.; Kim, S. J., Electrochemical graphene/carbon nanotube yarn artificial muscles. *Sensors and Actuators B: Chemical* **2019,** *286*, 237-242.
14. Qiao, J.; Di, J.; Zhou, S.; Jin, K.; Zeng, S.; Li, N.; Fang, S.; Song, Y.; Li, M.; Baughman, R. H.; Li, Q., Large-stroke electrochemical carbon nanotube/graphene hybrid yarn muscles. *Small* **2018,** *14* (38), 1801883.
15. Mu, J.; Jung de Andrade, M.; Fang, S.; Wang, X.; Gao, E.; Li, N.; Kim, S. H.; Wang, H.; Hou, C.; Zhang, Q.; Zhu, M.; Qian, D.; Lu, H.; Kongahage, D.; Talebian, S.; Foroughi, J.; Spinks, G.; Kim, H.; Ware, T. H.; Sim, H. J.; Lee, D.

Y.; Jang, Y.; Kim, S. J.; Baughman, R. H., Sheath-run artificial muscles. *Science* **2019,** *365* (6449), 150-155.

16. Lee, J. A.; Li, N.; Haines, C. S.; Kim, K. J.; Lepró, X.; Ovalle-Robles, R.; Kim, S. J.; Baughman, R. H., Electrochemically powered, energy-conserving carbon nanotube artificial muscles. *Advanced Materials* **2017,** *29* (31), 1700870.
17. Rogers, G. W.; Liu, J. Z., Monolayer graphene oxide as a building block for artificial muscles. *Applied Physics Letters* **2013,** *102* (2), 021903.
18. Rogers, G. W.; Liu, J. Z., High-performance graphene oxide electromechanical actuators. *Journal of the American Chemical Society* **2012,** *134* (2), 1250-1255.
19. Van Thanh, V.; Hung, N. T.; Van Truong, D., Charge-induced electromechanical actuation of Mo- and W-dichalcogenide monolayers. *RSC Advances* **2018,** *8* (67), 38667-38672.